



A new method for internal cooling of a large format lithium-ion battery pouch cell

O. Elsewify ^a, M. Soury ^b, M.N. Esfahani ^c, E. Hosseinzadeh ^d, M. Jabbari ^{a,*}

^a Department of Mechanical, Aerospace and Civil Engineering, University of Manchester, Manchester, M13 9PL, UK

^b Harvard John A. Paulson School of Engineering and Applied Sciences, Harvard University, Cambridge, MA, 02138, USA

^c Department of Electronic Engineering, University of York, York, YO10 5DD, UK

^d WMG, University of Warwick, Coventry, CV4 7AL, UK



ARTICLE INFO

Article history:

Received 14 August 2020

Received in revised form

9 February 2021

Accepted 17 February 2021

Available online 4 March 2021

Keywords:

Lithium-ion batteries

Internal cooling channel

Thermal management

Numerical modelling

ABSTRACT

In this paper a new battery thermal management system (BTMS) is proposed, where an internal cooling channel carrying water through the battery cells is integrated to a cell. A two-dimensional (2-D) thermal model is developed and validated against experimental data from literature for a 53 Ah lithium-ion battery (LIB) cell. The model is then adapted to reflect the installation of an internal cooling channel. The influence of different parameters such as the channel size, the channel location, and the inlet flow velocity on the thermal performance of the LIB cell is investigated. The results show that using optimal channel size with combination of best channel location as well as inlet velocity reduces the peak temperature by 26% and 20% for 3C and 5C discharge rates, respectively. Consequently, the average cell temperature is reduced by 24% for a 3C discharge rate, and 15% for a 5C discharge rate.

© 2021 Elsevier Ltd. All rights reserved.

1. Introduction

Electrically driven vehicles (EDVs) have emerged as the most suitable replacements for petrol cars and the vast majority of these vehicles are powered by lithium-ion battery (LIB) packs. One of the biggest challenges associated with LIB is that the operating temperature range is very narrow and there are significant safety risks that appear when functioning outside this range. For example, when temperature exceeds 80°C thermal runaway becomes a concern, as it causes harmful gas emissions, smoke, fires and possible explosions [1]. Furthermore, having the temperature gradient outside 5–7°C leads to detrimental effects on battery longevity and exacerbated degradation of the cells within a battery pack [2,3].

The heat generated within the battery cells is a function of charging and discharging processes, which impact the batteries' performance. Reducing these rates can solve some issues related to thermal challenges but limits the maximum power output. As such, one of the main focuses of EDV research is the development of thermal management systems to cool the battery cells within an optimal range. This facilitates reliable approaches to

overcome the safety and longevity concerns while drastically improving performance and simultaneously maintaining the level of power output [4].

There are currently two fundamental issues that electric vehicles must overcome to attain the ultimate performances. Firstly, there are functionality concerns; overheating of the power cells is commonplace and so is the shortage of battery life. Secondly, there are also significant safety concerns; thermal runaway regularly happens [5], and battery explosions are rare but pose a deadly risk to the public [6]. Hence, there has been a lot of research focused on various methods of battery thermal management system (BTMS) [7] — for example (forced) air cooling [8], liquid cooling [9,10], heat pipes [3], phase change material (PCM) [11,12], and conductive plate cooling [13,14].

Liquid cooling is effective technique using a liquid medium, such as water, which has a relatively good thermo-physical properties allowing for great temperature reductions at the battery surface [1,15]. However, liquid cooling systems are heavy and take up a lot of space, which is not ideal for heavy duty commercial use. Additional power to activate the pumping mechanism — referred as parasitic power — is another challenge in those systems. Liquid cooling system can be optimised using a graphite plate between the battery cell and the radiator pipes, which can reduce the temperature difference from 7°C to 2°C [1]. This is explained by the

* Corresponding author.

E-mail address: m.jabbari@manchester.ac.uk (M. Jabbari).

Nomenclature

1-,2-,3-D	1-,2-,3-dimensional
\bar{T}	Average temperature, °C
C/C-rate	Charge/discharge rate
h	Convective heat transfer coefficient, $W/m^2 \cdot ^\circ C$
I	Current, A
c_p	Heat capacity, $J/kg \cdot K$
\dot{q}''	Heat generation term, W/m^3
H	Height
N	Mesh resolution
\mathbf{n}	Normal vector
Nu	Nusselt number
U_{OCV}	Open circuit voltage of the cell
Pr	Prandtl number
R	Resistance, Ω
Re	Reynolds number
T	Temperature, °C
V_t	Terminal voltage
k	Thermal conductivity, $W/m \cdot ^\circ C$
t	Time, s
u	Velocity, m/s
W	Width

Greek Symbols

ρ	Density, kg/m^3
Ω	Domain
μ	Dynamic viscosity, $kg/m \cdot s$
Γ	Interface/Boundary

Subscripts

act	Active material
a	Aluminum
∞	Ambient (for temperature)
b	Battery active material
cell	Battery cell
tab	Battery tab
ch	Channel
c	Contact resistance, Ω
f, f	Fluid
max	Maximum
o	Ohmic resistance, Ω
OCV	Open circuit voltage

Superscripts

–	Negative tab
new	New dimension
old	Old dimension
+	Positive tab

Acronyms

Acc	Accuracy
Al	Aluminum
BTMS	Battery thermal management systems
EDV	Electrically driven vehicle
LIB	Lithium-ion battery
OCV	Open circuit voltage
PCM	Phase change material
SOC	State of charge

extremely high thermal conductivity of the graphite plate effectively improving the heat transfer efficiency of the system. Sheng et al. [16] developed a cooling jacket for cylindrical battery cells, which can capture a lower temperature standard deviation and a more even thermal profile. The benefit of such a design is that it is special conservative while maintaining a large contact profile with the cell surface. Lan et al. [17] examined the use of an aluminium mini-channel tube structure, which externally are surrounded by the prismatic LIB cells. These microchannels surrounded the cell on three of its four sides, and the temperature distribution across the battery was studied at different discharge rates. The report concluded that for a 2C discharge, using a liquid flow rate of 1 L/min, T_{max} is kept to 28.27°C and ΔT is 1.26°C. They also noted that further increasing the water flow rate would not reduce the temperature near the battery centre.

One solution to control the temperature levels is the installation of a PCM mandrel through the centre of a cylindrical LIB [18]. With the use of an aluminium mandrel containing paraffin as the PCM, the maximum temperature observed in a charging cycle can be reduced by 8.7°C. Gou et al. [18] concluded that regarding internal cell cooling, a combination of a heat pipe and phase change material within the cell is the most effective scheme, reducing the maximum temperature, T_{max} , to 33.8°C and ΔT to less than 0.9°C for 3C charging.

Zhao et al. [19] conducted a similar experiment, in which 18650 cylindrical batteries were filled with a mandrel containing phase change material. For their experiment, 40 LIBs were connected, and paraffin was used as the PCM. Using natural convection around the cells and the internal PCM core, the temperature difference ΔT can be kept to 2°C. They also concluded that the ideal setup to keep T_{max} below 40°C and ΔT below 5°C, is to use a PCM core of radius

3.2 mm in addition to external airflow at 1 m/s.

An et al. [20] placed 25 LIBs in an aluminium case surrounded by phase change material with liquid flow channels set within the PCM. Using water as the cooling fluid they found that increases in flow velocity beyond 0.8 m/s were unjustified and that the ideal flow velocity is 0.14 m/s. They also concluded that with the addition of 6 wt.% expanded graphite to the paraffin PCM in addition to 0.14 m/s flow, T_{max} is kept to 46.3°C and ΔT is only 2°C. However, the use of PCMs presents design engineers with a difficult encapsulation situation as the materials often do not conform to the available geometry [21]. Furthermore, during idle/standby the PCM releases energy back to the batteries increasing their temperatures offsetting their main purpose [22]. One way in which PCM usage can be improved is through the addition of a graphite composite with higher thermal conductivity. This improves temperature uniformity and charge/discharge performances achieved for the PCM [23]. Additionally, some promising efforts have been to create a hybrid active-passive cooling mechanism using both liquid and PCM cooling and have proven to reduce maximum temperatures and gradients considerably [24]. Wang et al. [25] explored the effects of PCM mixtures with nano-emulsions on the thermal management performances of lithium-ion battery packs. Their work found that mixtures with as little as 10 wt% OP28E were superior to that of water, reducing both the maximum temperatures and temperature gradients observed.

Moving forward it appears that internal cooling channels are the optimal BTMS for electric vehicle applications [13]. Mainly, this is due to the nature of its cooling, in which the hotspots within the battery cells are targeted to reduce the maximum temperature. Furthermore, liquid cooling involves much larger thermal conductivities compared to the use of PCM, this in turn allows for

greater heat exchange rates [13]. It is, therefore, the aim of this paper to investigate effective parameters on design and implementation of internal liquid cooling channel for an efficient thermal management system in LIB cells for EDV applications. Hence, this paper serves to address a gap in the open literature regarding the internal cooling of pouch/prismatic LIB cells.

2. Experimental cell specification

In this study commercial 53 Ah large format pouch cells ($x \times y \times z = 0.225 \text{ m} \times 0.225 \text{ m} \times 0.0118 \text{ m}$) manufactured by XALT ENERGY is used for validating the base 2-D model. The cathode chemistry is $\text{LiNi}_x\text{Mn}_y\text{Co}_{1-x-y}\text{O}_2$ (NMC) and the anode is made of graphite (LiC_6). The operating temperature range is between -20°C and 60°C for discharge, where the lower and upper limit voltage during discharge is 2.7 V. The open circuit voltage (OCV) was collected from the cells potential measurements during at 1C discharge from 100% to 0% SOC, in which 0% SOC corresponds to when the cut off voltage of 2.7 was reached. The cells were discharged for 144 s (0.04% SOC) at each single step accompanied by 4 h rest period. The terminal voltage of the cells was measured at the end of the rest periods. The measured OCV is shown in Fig. 1(a). The terminal voltage at 3C and 5C is also measured — see Fig. 1(b).

3. Methods

3.1. 2-D thermal model

This paper utilises a 2-D thermal model of the LIB cell during the discharge process — see Fig. 2. The 2-D model is selected because the thickness of the lithium-ion pouch cells in the z -direction is very small compared to the dimensions in the x - and y -directions [26]. As a result, the variation of temperature patterns through the z -direction are very small and can be neglected [11], making the 2-D model still accurate while reducing computational costs [27]. For this study the numerical model for the battery and the BTMS is implemented in MATLAB. This approach is taken as it allows for greater control of simulation parameters as well as providing greater flexibility in terms of the approach taken for results procurement. Furthermore, this also guarantees a high reproducibility of working conditions resulting in more reliable measured data [28]. MATLAB is chosen over commercial software such as ANSYS-Fluent or Abaqus because despite their high accuracy level, these type of commercial codes require an high degree of meshing and can be costly time-wise [26].

It is assumed that the cell bulk layer is homogeneous, which has effective values for heat capacity (c_p), density (ρ) and isotropic in-

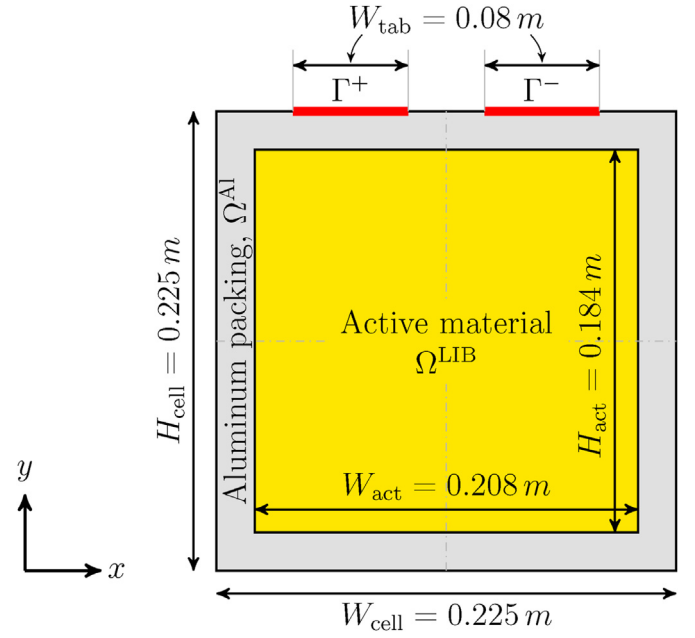


Fig. 2. Schematic illustration of a LIB cell (Ω^{LIB}) with surrounding aluminium packing (Ω^{Al}). All dimensions are based on [29].

plane thermal conductivity (k) [30,31] — as the thermal characteristics and stability of the active cell materials influences both the battery performance, as well as the operation temperature range [32]. The 2-D heat conduction equation for the LIB cell for calculating temperature (T), hence, becomes

$$\begin{cases} \rho_b c_{p,b} \frac{\partial T}{\partial t} = k_b \nabla^2 T + \dot{q}'' & \Omega \in \Omega^{\text{LIB}} \quad (a) \\ \rho_a c_{p,a} \frac{\partial T}{\partial t} = k_a \nabla^2 T & \Omega \in \Omega^{\text{Al}} \quad (b) \end{cases} \quad (1)$$

where the subscript b and a stand for battery and aluminium, respectively. The actual heat generation term consists of two parts, a reversible term and an irreversible term. The latter of which is due to the exothermic process associated with the discharge process, and increases with an increase in discharge rate [33,34]. By ignoring entropic heating and other modes of heat generation, the irreversible heat generation term becomes:

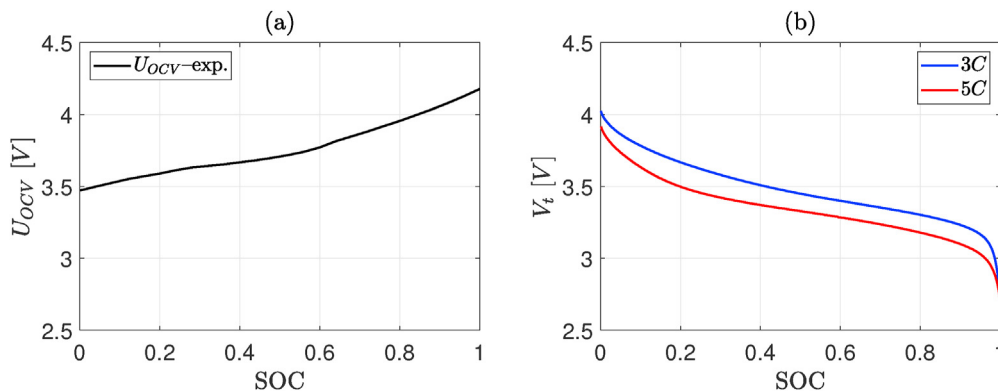


Fig. 1. Experimental measurements of (a) the cell OCV, and (b) the terminal voltage at the end of 3C and 5C discharge. All measurements are conducted at 25°C .

$$\dot{q}'' = \dot{q}_{\text{cell}}'' = I(U_{\text{OCV}} - V_t) \quad (2)$$

In this paper constant-current discharge is assumed and the variation of \dot{q}_{cell}'' obtained from the experimental data presented in Fig. 1, and for 3 and 5 discharge-rate (C-rate) the fitted functions are illustrated in Fig. 3. The boundary condition applied at the outer edge of the 2-D domain is

$$\begin{cases} k_a \frac{\partial T}{\partial \mathbf{n}} = \dot{q}_{\text{tab}}'' = (R_o^\Gamma + R_c^\Gamma) I^2 & \Gamma \in [\Gamma^+, \Gamma^-] \\ k_a \frac{\partial T}{\partial \mathbf{n}} = h_\infty (T - T_\infty) & \Gamma \notin [\Gamma^+, \Gamma^-] \end{cases} \quad (3)$$

in which k_a is the thermal conductivity of aluminium, \mathbf{n} is the normal vector, R_o is the ohmic resistance of the tabs, R_c is the contact resistance of the tabs, I is the current, h_∞ is the heat convection coefficient (assumed $6 \text{ W/m}^2 \cdot \text{K}$), and T_∞ is the surrounding temperature (that is set to 25°C in this study). For the boundary between the LIB and the aluminium packing, the thermal equilibrium is assumed at the interface enforcing the continuity of temperature

$$[T]^{\text{LIB}} = [T]^{\text{Al}} \quad (4)$$

as well as the continuity of heat fluxes across the boundary

$$[k_b \nabla T \cdot \mathbf{n}]^{\text{LIB}} = -[k_a \nabla T \cdot \mathbf{n}]^{\text{Al}} \quad (5)$$

Thermo-physical properties of the 53 Ah $\text{LiNi}_x\text{Mn}_y\text{Co}_{1-x-y}\text{O}_2$ (NMC) pouch cell as well as the aluminium packing are summarised in Table 1. The resistance values of the tabs are also listed in Table 2. All parameters listed in Tables 1 and 2 are based on [29,35].

3.2. Internal cooling channel

The internal channel cooling method proposed in this study is depicted in Fig. 4(a), where a cooling liquid (water in this study)

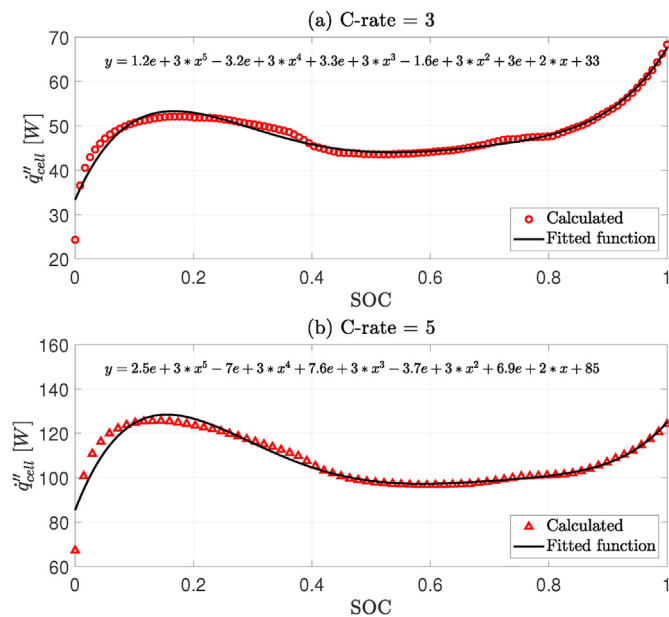


Fig. 3. Heat generation inside the 53 Ah LIB cell (under natural convection condition, $h_\infty = 6 \text{ W/m}^2 \cdot \text{K}$) and their corresponding fitted functions at different discharge rate of (a) 3C and (b) 5C.

Table 1

Thermo-physical properties of the 53 Ah NMC pouch cell [29,35], and the aluminium packing.

Material	ρ [kg/m ³]	c_p [J/kg·K]	k [W/m·K]
LIB	2551.7	1100	28
Al	2710	897	202

Table 2

Resistance values of the positive and negative tab as well as the 53 Ah NMC pouch cell [29,35].

Parameter	Negative tab	Positive tab
R_o [Ω]	3.48×10^{-5}	3.37×10^{-5}
R_c [Ω]	3.40×10^{-5}	6.37×10^{-5}

crosses through the LIB in the thickness direction. By including internal channel, in order for the battery to include the same active material as the base case, the length and width of the LIB cell is adjusted accordingly as follows

$$H_{\text{act}}^{\text{new}} = W_{\text{act}}^{\text{new}} = \sqrt{(W_{\text{act}}^{\text{old}} \times H_{\text{act}}^{\text{old}})} + (W_f \times H_f) \quad (6)$$

The 2-D model set-up for simulating internal cooling channel is illustrated in Fig. 4(b). Equations (1)–(5) are used to model temperature in the LIB and the aluminium packing domain. Inside the cooling channel the 2-D heat conduction model becomes

$$\rho_f c_{p,f} \frac{\partial T}{\partial t} = k_f \nabla^2 T \quad (7)$$

where ρ_f , $c_{p,f}$, and k_f are the density, heat capacity, and thermal conductivity of the cooling fluid, respectively. At the channel boundary with the LIB, heat convection is set as follows

$$k_f \frac{\partial T}{\partial \mathbf{n}} = h_f (T - T_f) \quad (8)$$

in which the heat transfer coefficient of the cooling fluid, h_f , is calculated using the below set of equations based on the thermo-physical properties as well as flow velocity of the cooling fluid — similar to Ref. [36].

$$\begin{cases} Re = \frac{\rho_f \times u \times W_f}{\mu_f}, & Pr = \frac{c_{p,f} \times \mu_f}{k_f} \\ Nu = 0.023 (Re^{0.8}) (Pr^{\frac{1}{3}}) \\ h_f = \frac{Nu \times k_f}{W_f} \end{cases} \quad (9)$$

and thermo-physical properties of water as cooling fluid inside the channel are summarised in Table 3.

3.3. Mesh sensitivity analysis

The simulation domain is discretised with a structured mesh, with the number of elements in x-direction, N_x (that is equal to the number of elements in y-direction, N_y). The average LIB cell temperature is evaluated by seven different mesh resolution, $N_x (= N_y)$, of 10, 20, 40, 60, 80, 100, and 120 — see Fig. 5. The results show that the simulation is independent of the mesh size where resolutions bigger than and equal to $N_x \times N_y = 80 \times 80$ are used.

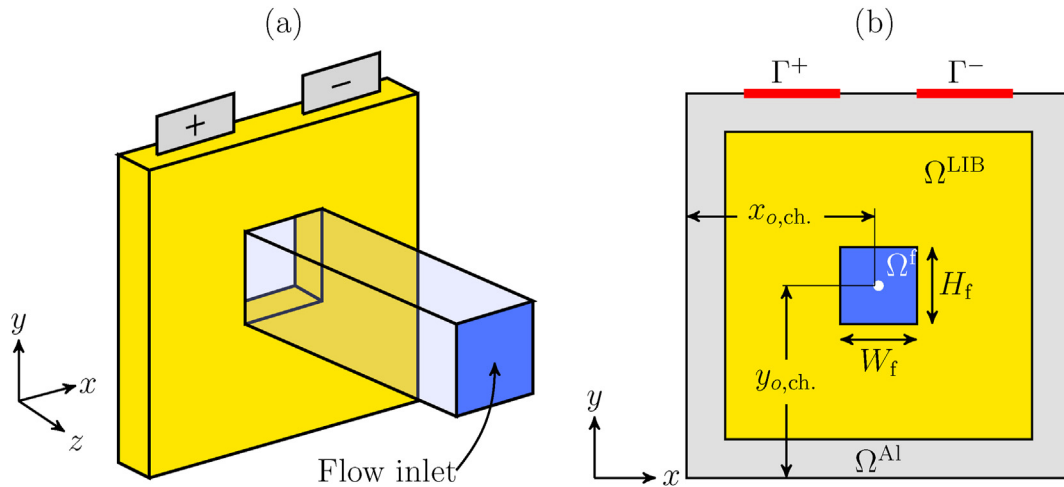


Fig. 4. (a) schematic illustration of a LIB cell with a cooling channel going through, and (b) 2-D model set-up with a single 2-D LIB cell (Ω^{LIB}) that interacts with a surrounding aluminium packing (Ω^{Al}) as well as an internal cooling channel (Ω^f).

Table 3

Thermo-physical properties of water as cooling fluid [37].

ρ_f [kg/m ³]	$c_{p,f}$ [J/kg·K]	k_f [W/m·K]	μ_f [kg/m·s]
990	4200	0.6	8.9×10^{-4}

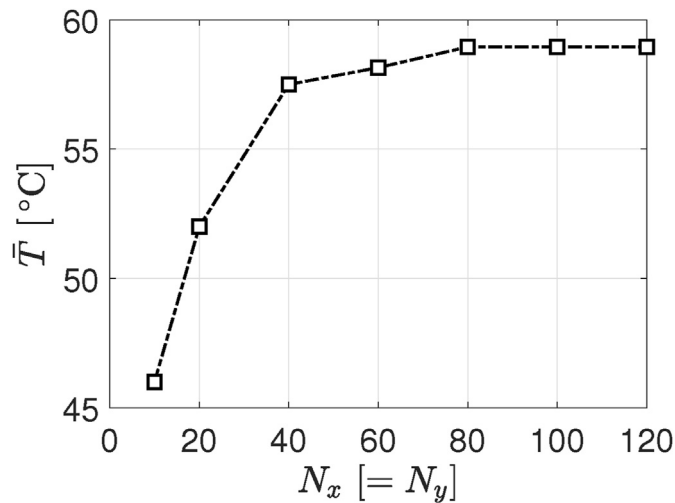


Fig. 5. Variation of the average LIB cell temperature with the mesh resolution. All results are for the 53 Ah cell at the end of 5C discharge event. Dashed lines are guides for the eyes.

4. Results and discussion

4.1. Base model validation

To confirm the accuracy as well as validity of the numerical model, its results are compared to thermal images published by Hosseinzadeh et al. [29]. The lab experiment conducted involved discharging the LIB cell at 3C and 5C discharging rates, and capturing thermal images at specified times during the discharge process. Fig. 6(a) and (b) present a comparison of the temperature contour from the MATLAB simulation and the contour produced through the experiment, for the 3C discharge case after 1100 s. The numerical results compare favourably with experimental findings

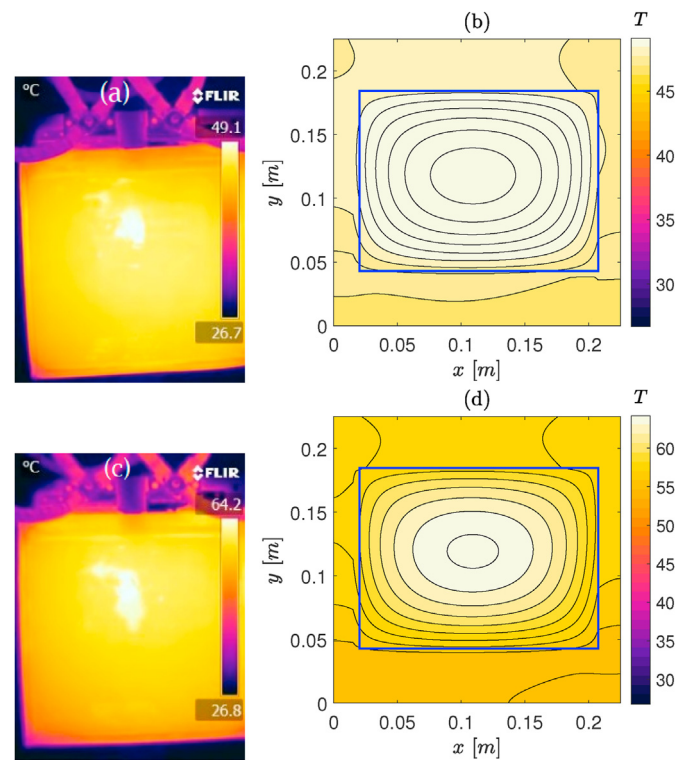


Fig. 6. Surface temperature distribution of the 53 Ah cell at 3C obtained from (a) thermal camera [29], and (b) numerical model (current study); and at 5C obtained from (c) thermal camera [29], and (d) numerical model (current study). The blue line in the numerical results illustrates the boundary between LIB and Al. (For interpretation of the references to colour in this figure legend, the reader is referred to the Web version of this article.)

both in terms of the peak temperature reached and the general trend spatially.

Similarly, Fig. 6(c) and (d) depict a comparison of the temperature contour from the MATLAB simulation and the contour produced through the experiment, for the 5C discharge case after 680 s. The result indicates that the numerical model is also accurate for the 5C discharge and the experimental data is accurately predicted. The simulation captures the magnitude and location of the

Table 4

Comparison of maximum temperature between experimental data [29] and numerical prediction from the current study, and the accuracy of the model.

C-rate	t [s]	$T_{\max}^{\text{exp.}}$ [°C]	$T_{\max}^{\text{num.}}$ [°C]	Acc. [%]
3	30	26.9	25.87	96.18
	400	36.1	36.51	98.87
	800	42.6	44.44	95.69
	1100	49.1	51.29	95.55
5	30	28.7	27.33	95.21
	100	35	33.68	96.24
	400	51.5	50.70	98.44
	680	64.2	64.21	99.99

peak temperature relatively accurately.

To replicate the thermal images reported by Hosseinzadeh et al. [29], the numerical model is run at 3C for 30, 400, 800 and 1100 s. This is also done for the 5C discharging rate and thermal plots are produced at 30, 100, 400 and 680 s. For each of the images produced, the colour bar scale is varied to match the corresponding thermal images. The accuracy of the model is then calculated using the following formula:

$$\text{Acc. (\%)} = \left(1 - \left| \frac{T_{\max}^{\text{image}} - T_{\max}^{\text{num.}}}{T_{\max}^{\text{image}}} \right| \right) \times 100 \quad (10)$$

Table 4 shows the accuracy for each of the 8 cases modelled by the numerical code. The average accuracy for this test is 97.02% with a standard deviation of 1.80%, with the least accurate test being the 3C discharge after 1100 s. The grid size used is 90×90 nodes. Results show the developed model agrees very well with the experimental data, and the maximum deviation is about 4.5%. This confirms that the base code is valid, and it will be used further for the internal cooling channel concept proposed in this study.

4.2. Internal cooling channel

4.2.1. Influence of channel size

There exists a significant correlation between the channel size and the maximum temperature observed, as the channel size is increased the T_{\max} value decreases — see Fig. 7(a). This can be expected as more fluid is passing through the cell, increasing the mass flow rate within the channel and hence allowing for greater heat transfer rates. However, in practical terms increasing the channel size to such a large extent can be detrimental to the cell performance as the active cell area around the channel is thinly distributed, which would affect the chemical reactions involved

during the discharge.

As the channel size is increased, an initial decrease in the temperature gradient is observed followed by an increase and a subsequent decrease — see Fig. 7(b). Ideally the channel that produces the lowest temperature gradient should be used, however, the trade-off in that case would be the T_{\max} value. Fig. 7(b) also illustrates that the change in dT is relatively small only 2 °C in the 3C case and 4 °C in the 5C case. As such not much improvement can be made to the temperature gradient by increasing the channel size. However, using a channel that is $0.04 \text{ m} \times 0.04 \text{ m}$, seems to be the optimal setup because it significantly reduces the maximum temperature while maintaining the active area integrity, and hence, it is used for further investigation for the rest of this paper.

4.2.2. Impact of channel position

In order to place the channel in the optimal position through the cell, an investigation is conducted to observe the changes in T_{\max} as the channel centre is moved in the x – direction from the left to right. As seen from Fig. 8(a), the optimal position for both 5C and 3C is at a distance of 0.1125 m, which correlates with the centre of the 0.225 m width of the cell. This result was expected as the centre point of the cell in the x direction is furthest from the left and right sides of the battery cell where natural convection can carry heat away.

The vertical position of the cooling channel is, moreover, changed to evaluate its influence on the cell temperature. Fig. 8(b) shows that variation of channel position in y – direction will also impact on the cooling performance of the internal channel. The results from the base model show that the hotspot of the battery cell is located at a height of 0.125 m from the bottom edge of the cell. It is seen from Fig. 8(b) that the temperature is lowest for both the 5C and 3C cases when the channel is placed at a height of 0.125 m. This indicates that the position of the hotspot does not change for the 3C and 5C discharge rate, so it is reasonable to fix the channel position at the 0.125 m height. Therefore, for the rest of the rest of the current paper $x_{0,\text{ch.}} = 0.1225 \text{ m}$ and $y_{0,\text{ch.}} = 0.125 \text{ m}$ are used for the internal channel position.

4.2.3. Cell temperature

Fig. 9(a) and (b) illustrate the temperature distribution in the LIB when the internal cooling channel is used. As mentioned earlier, water is used as coolant, and for the results presented $W_f \times H_f = 0.04 \text{ m} \times 0.04 \text{ m}$ is set with the y -centre of the channel located at $y_{0,\text{ch.}} = 0.125 \text{ m}$. It is seen that for both discharge rates (3C and 5C) the hotspot from the centre of the LIB is removed. Moreover, the overall temperature within the LIB has dropped

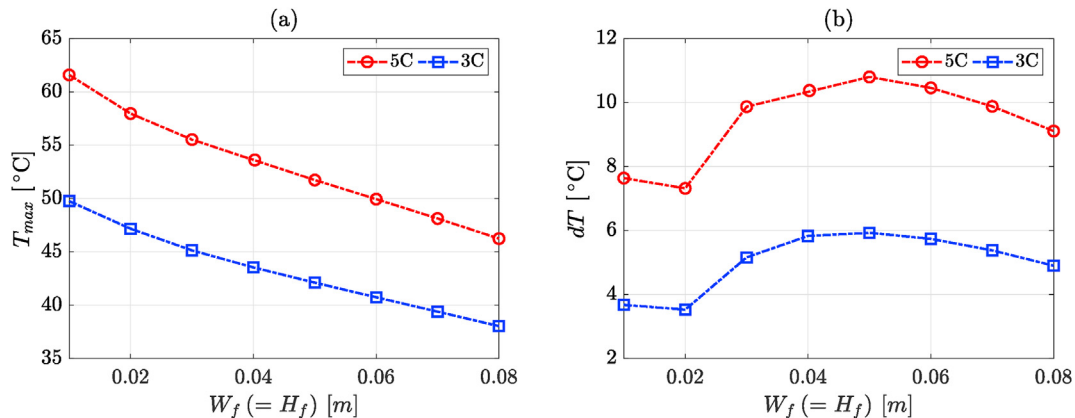


Fig. 7. Variation of (a) maximum temperature, and (b) temperature gradient with channel size at different discharge rate. All results are for $u = 1 \text{ m/s}$.

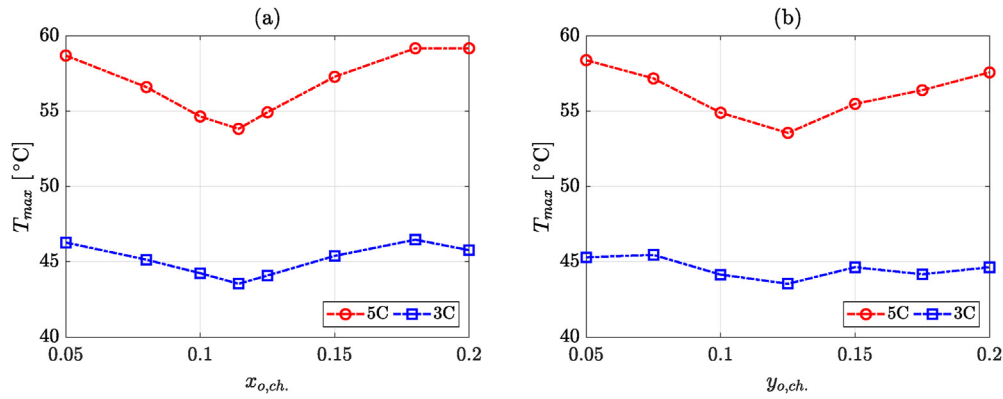


Fig. 8. Variation of maximum temperature with channel vertical position at different discharge rate of (a) 3C, and (b) 5C. All results are for $W_f \times H_f = 0.04 \text{ m} \times 0.04 \text{ m}$ and $u = 1 \text{ m/s}$.

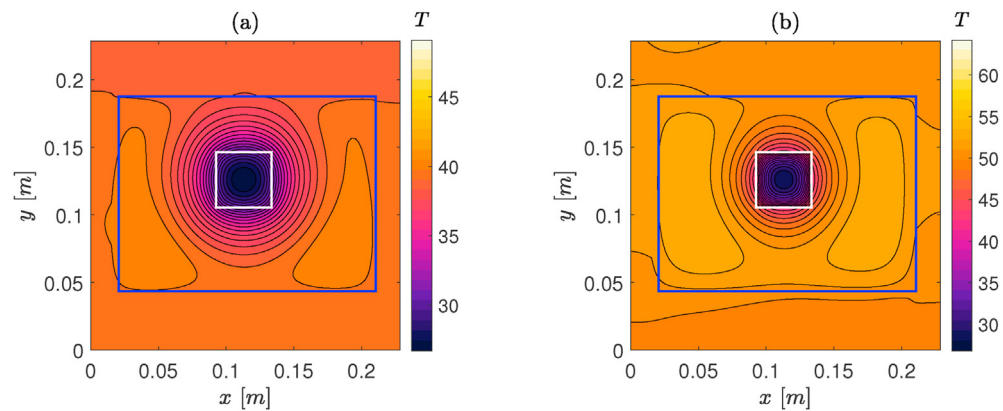


Fig. 9. Numerical results of surface temperature distribution of the 53 Ah cell with internal cooling channel and at different discharge rate of (a) 3C, and (b) 5C. Water velocity is set to $u = 1 \text{ m/s}$, and $y_{o, ch.} = 0.125 \text{ m}$ is used. The blue line shows the boundary between LIB and Al, and the white line represents the channel boundary. (For interpretation of the references to colour in this figure legend, the reader is referred to the Web version of this article.)

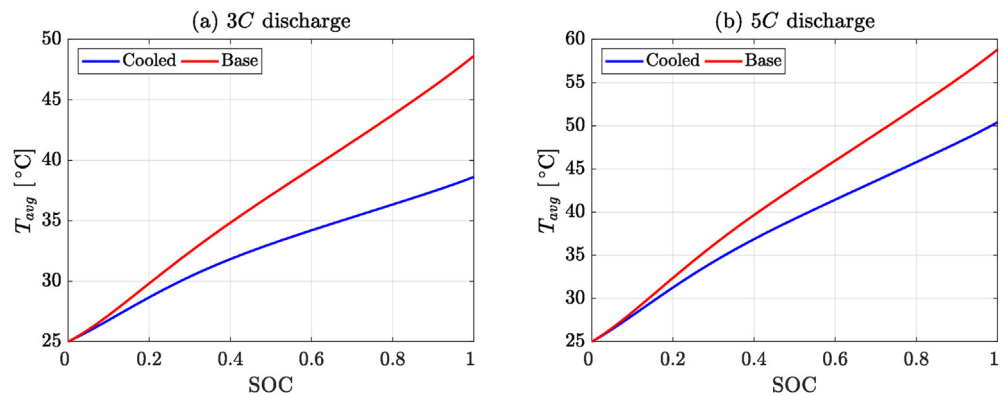


Fig. 10. Average temperature evolution during the (a) 3C, and (b) 5C discharge even. All results are for $y_{o, ch.} = 0.125 \text{ m}$ and $u = 1 \text{ m/s}$.

significantly (compared to the same condition without cooling channel in Fig. 6). Fig. 9(a) shows that adding the cooling channel for the 3C case addresses the issue of the central hotspot within the cell, and as a result the maximum temperature drops to 40.68 °C. Importantly, the maximum temperature measured for the 5C discharge event drops by 10.65 °C, which is significant improvement on the normal operating conditions. The results confirms the effectiveness of the cooling channel as a thermal management system, and how it addresses the issue of a central hotspot within the cell as well as reducing the cell temperature.

The evolution of cell average temperature at different discharge rate is illustrated in Fig. 10(a) and (b). The results show that integration of internal cooling channel has a more pronounced effect at the later stages of the discharge process than the earlier parts. For the 5C discharge, the average cell temperature drops by 7.79 °C, from 58.82 °C to 51.03 °C, which is within the safe operating range for lithium-ion cells. It is, moreover, seen that for the 3C case study, the effect of the channel is most noticeable by dropping the average cell temperature from 48.63 °C to 39.13 °C.

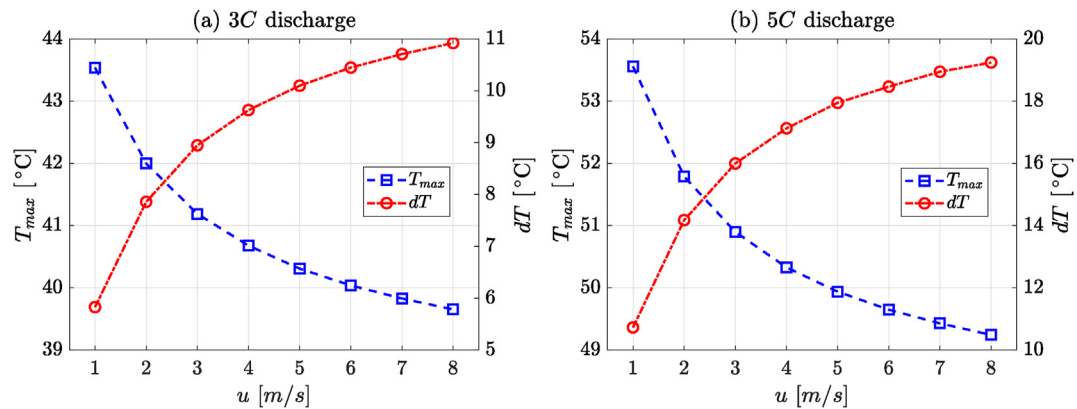


Fig. 11. Effect of channel flow velocity on the maximum cell temperature and temperature gradient for (a) 3C, and (b) 5C. All results are for $y_{o, ch.} = 0.125$ m.

4.2.4. Impact of flow velocity in the channel

The next step is to vary the velocity of the flow through the channel in order to optimise cooling effect. It is expected that as the channel flow velocity is increased the maximum cell temperature will decrease because the fluid can carry heat away from the cell at a faster rate [38]. This is captured by the present model and illustrated in Fig. 11(a) and (b) for 3C and 5C discharge event, respectively. The addition of the cooling channel can, however, be detrimental to the temperature gradients observed within the cell because the channel imposes a steep temperature gradient at the channel/active area interface. This temperature gradient must be kept low to reduce cell degradation and prolong battery life [2,3]. As such it is necessary to select a relatively lower velocity which will reduce the peak temperature while keeping the temperature difference low. Based on the current results, the flow velocity above 2 m/s is not recommended.

5. Conclusion

In this paper a 2-D thermal model is developed to simulate the temperature distribution in a 53 Ah LIB pouch cell, and validated against recently published results from literature. The model is then further used for simulating a new proposed internal cooling channel, where water (as a cost-effective cooling medium) is transferring heat away from the battery cell by a channel going through the cell. Several parameters are varied and optimised in order to find the most effective cooling method, and a summary of these investigations is listed below.

- The optimal position for the installation of a cooling channel is at a height of $y_{o, ch.} = 0.125$ m from the bottom edge of the cell and a distance of $x_{o, ch.} = 0.1125$ m from the cell left edge.
- Increasing the velocity of the flow within the channel reduces the maximum (and average) cell temperatures but increases the temperature gradient within the cell. The optimal velocity is predicted to be less than and equal to 2 m/s both 3C and 5C discharge rates.
- Using the proposed approach, the peak temperature is reduced by 26% and 20% for 3C and 5C discharge rates, and the average cell temperature is reduced by 24% and 15% for a 3C and 5C discharge rate, respectively.

The developed model in this study is used to evaluate thermal performance of a single LIB cell. Extending the current model to multiple cells and/or module/pack level may be of interest for future studies. Altering the fluid inside the internal cooling channels (with nanofluids for instance) could be another interesting phenomenon to investigate.

Credit author statement

Omar Elsewify: Conceptualization, Methodology, Software, Validation, Formal analysis, Investigation, Writing – original draft, Visualization. Mohammad Sour: Writing – review & editing, Supervision. Mohammad Nasr Esfahani: Writing – review & editing, Supervision. Elham Hosseinzadeh: Validation, Writing – review & editing, Supervision. Masoud Jabbari: Conceptualization, Methodology, Investigation, Writing – review & editing, Supervision.

Declaration of competing interest

The authors declare that they have no known competing financial interests or personal relationships that could have appeared to influence the work reported in this paper.

References

- [1] Deng Y, Feng C, Jiaqiang E, Zhu H, Chen J, Wen M, Yin H. Effects of different coolants and cooling strategies on the cooling performance of the power lithium ion battery system: a review. *Appl Therm Eng* 2018;142:10–29.
- [2] Yang N, Zhang X, Shang B, Li G. Unbalanced discharging and aging due to temperature differences among the cells in a lithium-ion battery pack with parallel combination. *J Power Sources* 2016;306:733–41.
- [3] Worwood D, Kellner Q, Wojtala M, Widanage W, McGlen R, Greenwood D, Marco J. A new approach to the internal thermal management of cylindrical battery cells for automotive applications. *J Power Sources* 2017;346:151–66.
- [4] Peterson SB, Apt J, Whitacre J. Lithium-ion battery cell degradation resulting from realistic vehicle and vehicle-to-grid utilization. *J Power Sources* 2010;195(8):2385–92.
- [5] Tourani A, White P, Ivey P. Analysis of electric and thermal behaviour of lithium-ion cells in realistic driving cycles. *J Power Sources* 2014;268:301–14.
- [6] Liu B, Jia Y, Yuan C, Wang L, Gao X, Yin S, Xu J. Safety issues and mechanisms of lithium-ion battery cell upon mechanical abusive loading: a review. *Energy Storage Mater* 2020;24:85–112.
- [7] Kim J, Oh J, Lee H. Review on battery thermal management system for electric vehicles. *Appl Therm Eng* 2019;149:192–212.
- [8] Fan L, Khodadadi J, Pesaran A. A parametric study on thermal management of an air-cooled lithium-ion battery module for plug-in hybrid electric vehicles. *J Power Sources* 2013;238:301–12.
- [9] Panchal S, Khasow R, Dincer I, Agelin-Chaab M, Fraser R, Fowler M. Thermal design and simulation of mini-channel cold plate for water cooled large sized prismatic lithium-ion battery. *Appl Therm Eng* 2017;122:80–90.
- [10] Patil MS, Seo J-H, Panchal S, Jee S-W, Lee M-Y. Investigation on thermal performance of water-cooled li-ion pouch cell and pack at high discharge rate with u-turn type microchannel cold plate. *Int J Heat Mass Tran* 2020;155: 119728.
- [11] Qu Z, Li W, Tao W. Numerical model of the passive thermal management system for high-power lithium ion battery by using porous metal foam saturated with phase change material. *Int J Hydrogen Energy* 2014;39: 3904–13.
- [12] Choudhari V, Dhoble A, Panchal S. Numerical analysis of different fin structures in phase change material module for battery thermal management system and its optimization. *Int J Heat Mass Tran* 2020;163:120434.
- [13] Chen D, Jiang J, Kim G-H, Yang C, Pesaran A. Comparison of different cooling methods for lithium ion battery cells. *Appl Therm Eng* 2016;94:846–54.
- [14] Jabbari M, Wang R, Liang Z, Esfahani M, Hosseinzadeh E. Numerical modelling

- of nanocomposite conductive plate for battery thermal management using a novel multi-domain approach. *Appl Therm Eng* 2021;182:116067.
- [15] Cao J, Luo M, Fang X, Ling Z, Zhang Z. Liquid cooling with phase change materials for cylindrical li-ion batteries: an experimental and numerical study. *Energy* 2020;191:116565.
 - [16] Sheng L, Zhang H, Su L, Zhang Z, Zhang H, Li K, Fang Y, Ye W, Statement CA. Effect analysis on thermal profile management of a cylindrical lithium-ion battery utilizing a cellular liquid cooling jacket. *Energy* 2020;119725.
 - [17] Lan C, Xu J, Qiao Y, Ma Y. Thermal management for high power lithium-ion battery by minichannel aluminum tubes. *Appl Therm Eng* 2016;101:284–92.
 - [18] Gou J, Liu W, Luo Y. The thermal performance of a novel internal cooling method for the electric vehicle battery: an experimental study. *Appl Therm Eng* 2019;161:114102.
 - [19] Zhao R, Gu J, Liu J. Optimization of a phase change material based internal cooling system for cylindrical li-ion battery pack and a hybrid cooling design. *Energy* 2017;135:811–22.
 - [20] An Z, Chen X, Zhao L, Gao Z. Numerical investigation on integrated thermal management for a lithium-ion battery module with a composite phase change material and liquid cooling. *Appl Therm Eng* 2019;163:114345.
 - [21] Farid MM, Khudhair AM, Razack SAK, Al-Hallaj S. A review on phase change energy storage: materials and applications. *Energy Convers Manag* 2004;45(9–10):1597–615.
 - [22] Zhang X, Kong X, Li G, Li J. Thermodynamic assessment of active cooling/heating methods for lithium-ion batteries of electric vehicles in extreme conditions. *Energy* 2014;64:1092–101.
 - [23] Jiang L, Zhang H, Li J, Xia P. Thermal performance of a cylindrical battery module impregnated with pcm composite based on thermoelectric cooling. *Energy* 2019;188:116048.
 - [24] Fathabadi H. High thermal performance lithium-ion battery pack including hybrid active–passive thermal management system for using in hybrid/electric vehicles. *Energy* 2014;70:529–38.
 - [25] Wang F, Cao J, Ling Z, Zhang Z, Fang X. Experimental and simulative investigations on a phase change material nano-emulsion-based liquid cooling thermal management system for a lithium-ion battery pack. *Energy* 2020;207:118215.
 - [26] Samba A, Omar N, Gualous H, Firouz Y, Van den Bossche P, Van Mierlo J, Boubekeur TI. Development of an advanced two-dimensional thermal model for large size lithium-ion pouch cells. *Electrochim Acta* 2014;117:246–54.
 - [27] Alipanah M, Li X. Numerical studies of lithium-ion battery thermal management systems using phase change materials and metal foams. *Int J Heat Mass Tran* 2016;102:1159–68.
 - [28] Menale C, D'Annibale F, Mazzarotta B, Bubbico R. Thermal management of lithium-ion batteries: an experimental investigation. *Energy* 2019;182:57–71.
 - [29] Hosseinzadeh E, Genieser R, Worwood D, Barai A, Marco J, Jennings P. A systematic approach for electrochemical-thermal modelling of a large format lithium-ion battery for electric vehicle application. *J Power Sources* 2018;382:77–94.
 - [30] Chacko S, Chung YM. Thermal modelling of li-ion polymer battery for electric vehicle drive cycles. *J Power Sources* 2012;213:296–303.
 - [31] Xie Y, He X-j, Hu X-s, Li W, Zhang Y-j, Liu B, Sun Y-t. An improved resistance-based thermal model for a pouch lithium-ion battery considering heat generation of posts. *Appl Therm Eng* 2020;164:114455.
 - [32] Miranda D, Almeida A, Lanceros-Méndez S, Costa C. Effect of the active material type and battery geometry on the thermal behavior of lithium-ion batteries. *Energy* 2019;185:1250–62.
 - [33] Lai Y, Du S, Ai L, Ai L, Cheng Y, Tang Y, Jia M. Insight into heat generation of lithium ion batteries based on the electrochemical-thermal model at high discharge rates. *Int J Hydrogen Energy* 2015;40:13039–49.
 - [34] Lin C, Xu S, Liu J. Measurement of heat generation in a 40 ah lifepo4 prismatic battery using accelerating rate calorimetry. *Int J Hydrogen Energy* 2018;43:8375–84.
 - [35] Hosseinzadeh E, Marco J, Jennings P. Combined electrical and electrochemical-thermal model of parallel connected large format pouch cells. *J Energy Storage* 2019;22:194–207.
 - [36] Ma Y, Mou H, Zhao H. Cooling optimization strategy for lithium-ion batteries based on triple-step nonlinear method. *Energy* 2020;201:117678.
 - [37] Kestin J, Sengers J, Kamgar-Parsi B, Sengers JL. Thermophysical properties of fluid d2o. *J Phys Chem Ref Data* 1984;13(2):601–9.
 - [38] Yetik O, Karakoc TH. A numerical study on the thermal performance of prismatic li-ion batteries for hibrid electric aircraft. *Energy* 2020;195:117009.